Wear 300 (2013) 96–104

Contents lists available at SciVerse ScienceDirect

Wear

journal homepage: www.elsevier.com/locate/wear

Stability criteria for a pyramidal shaped asperity ploughing through a plastically deforming substrate

G. van der Linde [a], M.B. de Rooij [b,*], D.J. Schipper [b]

[a] Materials innovation institute (M2i), Delft, The Netherlands
[b] University of Twente, Laboratory of Surface Technology & Tribology, The Netherlands

ARTICLE INFO

Article history:
Received 13 July 2012
Received in revised form
29 November 2012
Accepted 24 January 2013
Available online 8 February 2013

Keywords:
Abrasive wear
Adhesive wear
Galling
Contact models
Plasticity

ABSTRACT

In two body abrasion processes hard asperities plough through a soft surface. If the asperities can resist the forces that act on it, scratches will develop in the soft material. If the asperities cannot withstand these forces, they will break off and not cause direct abrasion damage. The same is the case for galling, where lumps develop on one of the surfaces because of material transfer. These lumps will abrade the counter surface, if the lumps are strong enough to withstand the forces that act on it. In order to describe these phenomena, simple criteria are desired to describe the mechanical stability of asperities and lumps.

In this work, an analytical model is presented for the mechanical stability of asperities. In the analysis, a pyramidal asperity shape will be assumed. Given the pyramidal asperity shape, several cases will be studied: the load is carried by a pyramid with a triangular base, a pyramid with a triangular base and an extended backside and the case where a crack has developed. Based on these models stability criteria of ploughing pyramidal asperities will be developed. Important results of the model will be discussed in the context of abrasion and adhesive wear processes.

1. Introduction

Two body abrasion is a very common wear process in which harder asperities plough through a softer surface. Also in some adhesive wear processes harder asperities plough through a softer counter surface. Here, in time, ploughing asperities can grow and develop into larger lumps due to adhesion or mechanical locking of soft material into the surface roughness of the harder surface. The transferred material work hardens and can cause scratches in the countersurface. In particular when high lumps can develop, scratches will be formed on the product due to abrasion. An example of such an adhesive wear process followed by subsequent abrasion, is galling in a deep drawing process. In the case of galling, the geometry of the developing lumps will determine the depth and width of the scratches which develop due to ploughing. Because galling can be detrimental for the surface quality of the products being made, it is important to control it in industrial practice. The main difference with two body abrasion is that in this case the shape of the ploughing asperity is not fixed beforehand, but dependent on the growth behaviour of the transferred material on the asperity.

Modelling of abrasive wear has often started with analysing a single asperity ploughing through a soft and flat substrate. Analysis of single ploughing asperities is then extended to rough surfaces by summing up these unit events, see e.g. [1,2]. In such models, single asperity behaviour as discussed above is typically used and applied to multi asperity contacts. Further, it is typically assumed that the asperities are rigid, so strong enough to withstand the forces that act on them during ploughing. Several reasons exist which limit the validity of the assumption of a rigid asperity and therefore neglect failure of the asperity. Single asperity ploughing has been extensively studied in experiments as well as in models. An overview of many studies is given in [3]. Much of the work on ploughing asperities has been restricted to 2D situations. Important is the work described in [4] where ploughing of 2D wedges is modelled by means of slipline models. Using these models, three slipline fields have been defined, identified with the names: wave formation, wave removal and cutting. Depending on the attack angle of the wedge and the strength of the interface between the wedge and the deforming material, the wedge will operate in a certain mode. The transitions between these regimes have been related to wear modes of spherical asperities by Hokkirigawa and Kato [5]. There, on the basis of experiments and a comparison with the slipline models of Challen and Oxley [4] a wear mode diagram is constructed in which three wear modes are distinguished: ploughing, wedging and cutting. This diagram is schematically depicted in Fig. 1 and

* Corresponding author. Tel.: +31 534891178; fax: +31 534894784.
E-mail address: m.b.derooij@ctw.utwente.nl (M.B. de Rooij).

0043-1648/$ - see front matter © 2013 Elsevier B.V. All rights reserved.
http://dx.doi.org/10.1016/j.wear.2013.01.119

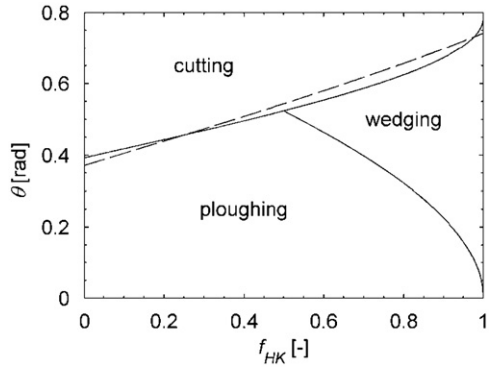

Fig. 1. Wear mode diagram according to Hokkirigawa and Kato [5].

will be discussed further. The transitions between the cutting regime and the other regimes are approximately given by the following equations, see also [6]:

$$\theta = 0.25(\pi - \arccos f_{HK}) \tag{1}$$

And the boundary between the ploughing and wedging regime is given by:

$$\theta = 0.5 \arccos f_{HK} \tag{2}$$

In these equations, θ is the attack angle of the sliding wedge and $f_{HK}=\tau/k$, where τ is the shear strength of the interface at the ploughing wedge and k is the shear strength of the soft plastically deforming counter surface. These equations are represented by the solid lines in Fig. 1. The dotted line is the exact boundary between the regimes which follows from [7]. It can be seen that the approximate relation is indeed very close to the exact solution. Next to ploughing wedges and spherical tips, ploughing cones [8] and pyramidal indenters [9,10] have also been analysed using the upper bound method. However, slipline models have some restrictions originating from the model assumptions. The most important restrictions are the neglect of elastic effects and the assumption of pure plastic material behaviour. So, at very small contact angles no ploughing is expected but elastic behaviour. In [16,17] limits due to elasticity have been analysed when indenting a plastically deforming substrate with a symmetric rigid wedge. If the criterion is applied to steel, elastic effects can be expected at attack angles lower than 18° for wedge shaped indenters. The criterion in fact represents the strain in the material due to indenting. When the results in the ploughing regime are compared with elastic–plastic FEM calculations, slipline solutions only give good results for attack angles higher than approximately 5° see [11]. The reason is that much higher strains than predicted by the slipline models develop close to the surface in the case of a ploughing wedge.

Secondly, failure of the ploughing tip itself can occur when sliding against a softer surface due to mechanical overloading despite its higher hardness. In [18,19] criteria are derived in terms of a critical tip angle for the sliding wedge and the hardness ratio between the sliding wedge and the softer flat.

Some of the basic assumptions like ideal plasticity of the soft surface and rigid behaviour of the hard asperity can be avoided using FEM models of ploughing asperities, one of the first being [11]. Later a single asperity moving over a countersurface has been simulated using meshless methods [12–15]. In these simulations, aspects like deformation of the ploughing asperity and material transfer to the ploughing asperity have been observed.

In this work, stability of pyramidal shapes will be investigated when ploughing through a plastically deforming material, using analytical models.

2. Modelling failure of asperities

2.1. Stress analysis for a simple triangular pyramid

Starting from a pyramidal asperity with a four sided base, only the front half will be in contact with the plastically deforming soft surface. The resulting geometry is a simple triangular pyramid loaded with forces due to the ploughing action of faces *BCD* and *ACD* as depicted in Fig. 2. If, only the front half of the four sided base supports the ploughing asperity, the asperity is supported by face *ABC*. Before discussing more complex situations, first this simple geometry will be analysed further.

The points *B* and *D* are respectively the extremes of the width *w* and the height *h*. The velocity vector of the moving soft counter surface relative to the fixed asperity is assumed to be acting in the negative *x*-direction. If a scratch is formed due to the ploughing action, behind the plane *ADB* no contact is expected. In reality the internal stress distribution is also dependent on the rear part of the asperity as will be discussed later. In the following, it will be assumed that the asperity is stationary and rigid with a plane of symmetry in the *xz*-plane. The asperity is loaded on face *BCD* (and because of the symmetry on face *ACD*) because of the ploughing action. Further, the rigid asperity is supported by face *OBC* (and because of the symmetry face *OAC*). In the analysis, the pressure p_{BCD} acting on face *BCD* will be called p_{pl}. p_{pl} is assumed to be constant over the whole contact area and directed inward normal to plane *BCD*. The tangential shear stress τ_{pl} is calculated using a Coulomb friction law, so $\tau_{pl} = \mu_{p_{pl}}$.

The geometry of the asperity is completely defined by *w*, *h* and the length *l* or in the dimensionless form, normalizing by *l*, two geometrical quantities remain

$$\overline{h} = \frac{h}{l} \tag{3}$$

$$\overline{w} = \frac{w}{l} \tag{4}$$

The coordinates of three points *B*, *D* and *C* are respectively given by (0, *w*, 0), (0, 0, *h*) and (*l*, 0, 0). These points describe a plane, which has the unit normal vector which will be denoted by n_{BCD}. The area of the triangle *BCD* is called A_{BDC}, and the area of triangle *ABC* is called A_{ABC} are given by

$$A_{BDC} = 1/2|BD \times BC| = 1/2\sqrt{(wh)^2+(hl)^2+(lw)^2} \tag{5}$$

$$\vec{n}_{BDC} = \frac{(wh, hl, lw)}{\sqrt{(wh)^2+(hl)^2+(lw)^2}} \tag{6}$$

$$A_{ABC} = wl \tag{7}$$

In the far field, the velocity vector is directed into the negative *x*-direction. The vector $\vec{t}$ is the tangent vector of *BDC* as close as possible to the direction of the plastic flow in the far field, so $\vec{x} \cdot \vec{t}$ has to be minimum. To minimize $\vec{x} \cdot \vec{t}$, vector $\vec{t}$ has to be

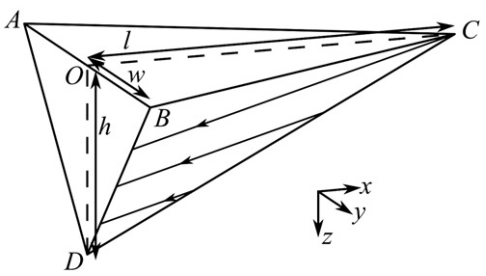

Fig. 2. Tip geometry with its dimension and flow lines on *BDC* of plastic deforming material.

in the plane that is described by the vectors $\vec{x}$ and $\vec{n}_{BDC}$. This results in

$$\vec{t} = \sqrt{\frac{w^2+h^2}{(wh)^2+(hl)^2+(lw)^2}}\left(-l,\ h\frac{wh}{w^2+h^2},\ w\frac{wh}{w^2+h^2}\right) \tag{8}$$

This tangent is illustrated in Fig. 2 by the lines with arrows on face *BDC*. The connection of the asperity to the bulk material at face *ABC* is assumed to be an elastic spring, normal to face *ABC*. This results in a constant tangential stress τ_{ABC} in the *x*-direction and a linear function in terms of *x* for the normal stress σ_{ABC}. Of importance for σ_{ABC} is the spring stiffness C_2, the deformation δ_0 at $x=0$ and the angle θ between plane *ABC* and the support. In summary, the following expressions for the stresses acting at face *ABC* are used:

$$\tau_{ABC} = C_1 \tag{9}$$

$$\sigma_{ABC} = -C_2(\delta_0+\theta x) \tag{10}$$

The forces in *y*-direction cancel out because of symmetry. Force equilibrium in respectively the *x*-direction and *z*-direction and moment equilibrium around the *y*-axis gives

$$\sum F_x = 0 \Rightarrow -\int p_{pl}\vec{n}\cdot\vec{x}\ dA + \int \tau_{pl}\vec{t}\cdot\vec{x}\ dA + \int \tau_{ABC}\ dA = 0 \tag{11}$$

$$\sum F_z = 0 \Rightarrow -\int p_{pl}\vec{n}\cdot\vec{z}\ dA + \int \tau_{pl}\vec{t}\cdot\vec{z}\ dA + \int \sigma_{ABC}(x)\vec{n}\cdot\vec{z}\ dA = 0 \tag{12}$$

$$\sum M_{yy} = 0 \Rightarrow \left(\int \vec{r}\times d\vec{F}\right)\cdot\vec{y} = \int z\,dF_x - \int x\,dF_z = 0 \tag{13}$$

This can be shown to result in the following expressions for σ_{ABC} and τ_{ABC}, see also Appendix A:

$$\frac{\tau_{ABC}}{p_{pl}} = \frac{1}{\bar{A}_{ABC}}\left(\bar{w}\bar{h}+\mu\sqrt{\bar{w}^2+\bar{h}^2}\right) \tag{14}$$

$$\frac{\sigma_{ABC}}{p_{pl}} = -\frac{\bar{w}}{\bar{A}_{ABC}}\left(1-\frac{\mu\bar{w}\bar{h}}{\sqrt{\bar{w}^2+\bar{h}^2}}\right)+\frac{1}{3\bar{I}_{cyy}} \times\left(\bar{w}(\bar{h}^2-1+3\bar{x}_c)+\frac{\mu\bar{h}(2\bar{w}^2+\bar{h}^2-3\bar{x}_c\bar{w}^2)}{\sqrt{\bar{w}^2+\bar{h}^2}}\right)(\bar{x}-\bar{x}_c) \tag{15}$$

In these expressions, dimensionless geometrical properties are used. Lengths, areas and area moments are normalized by respectively *l*, l^2 and l^4. This results in a dimensionless width $\bar{w}$, dimensionless height $\bar{h}$, *x*-coordinate of the centroid $\bar{x}_c$ dimensionless area $\bar{A}_{ABC}$ and area moment of inertia $\bar{I}_{cyy}$. This formulation makes the equations more general when applied to other geometries as will be shown below.

In the analysis presented above, the emphasis is on an accurate description of the stresses on the faces of the ploughing asperity rather than an accurate description of the flow field as is done in a more conventional upperbound analysis. Although the direction of the shear stresses according to Eq. (8) is approximate, the flow field has realistic characteristics. For blunt asperities the flow of material will be underneath the ploughing asperities while for sharp asperities, the material will flow along the sides of the ploughing asperity. For intermediate situations, there will be a gentle transition from one extreme to the other extreme situation. These results are in agreement with the reality of a ploughing asperity. The direction of the shear stress acting on the ploughing faces is therefore considered to be a good approximation and is considered to be sufficiently accurate to analyse the failure behaviour of the ploughing asperity.

2.2. Stress analysis for a triangular pyramid including an extended base at the back side and a crack at the front side

Although only the front part of the pyramid will be loaded because of ploughing, the tip can also experience support from material at the back of plane *ABD*. In order to model support by this area the geometry will be extended with the triangular support area *ABE*, see Fig. 3. If this area also contributes to the support, area *ABE* will be likely to experience compressive normal stresses due to the tilting moment caused by the loaded faces *BCD* (and *ACD*).

It can be shown that Eqs. (14) and (15) remain valid with new expressions for the terms $\bar{x}_c$, $\bar{A}_{ABC}$and $\bar{I}_{cyy}$ [6] and are given by

$$A_{ABC} = w(l+l_b) \tag{16}$$

$$x_c = \frac{w}{3A_{ABC}}(l^2-{l_b}^2) \tag{17}$$

$$I_{yy} = \frac{w}{6}(l^3+{l_b}^3) \Rightarrow I_{cyy} = \int (x-x_c)^2 dA = \int x^2 dA - {x_c}^2 A_{ABC} = I_{yy} - {x_c}^2 A_{ABC} \tag{18}$$

In this equation x_c is the *x*-coordinate of the centroid and A_{ABC} is the area of the face *ABC*. In order to further generalize the approach, also a crack will be assumed in the front part of the sliding asperity, so close to point C. The crack is supposed to be in the face *ABC* and starts at vertex *C* and has length l_{cr}, see Fig. 4.

The plastic forces on the faces *BDC* and *ACD* are not changed, but only the internal bearing area of face *ABC* (or *AEBC*). Also in this case, the same expressions as in Eqs. (14) and (15) can be used, but again with different expressions for A_{ABC}, x_c and I_{yy} according to, see [6]

$$A_{ABC} = w\left(l\left(1-\frac{l_{cr}}{l}\right)\left(1+\frac{l_{cr}}{l}\right)+l_b\right) \tag{19}$$

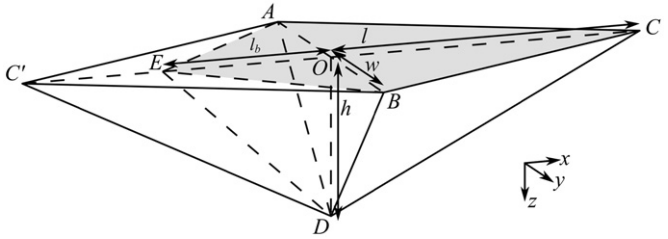

Fig. 3. Tip geometry with the extended base *AC'BC*. The grey quadrilateral *AEBC* is the region that (mainly) carries the plastic forces.

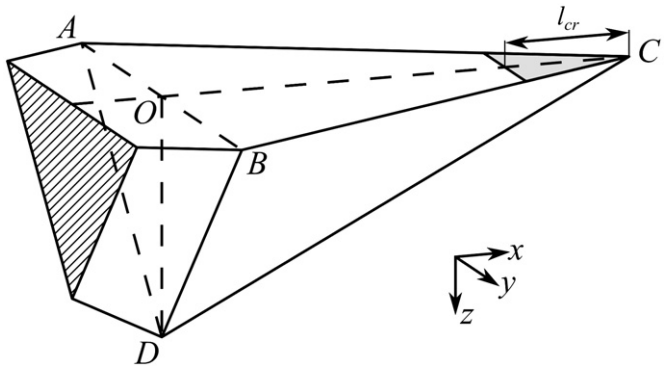

Fig. 4. Part of tip geometry with crack at vertex *C*.

$$x_c = \frac{w}{3A_{ABC}}\left(l^2\left(1-\frac{l_{cr}}{l}\right)^2\left(1+2\frac{l_{cr}}{l}\right)-{l_b}^2\right) \tag{20}$$

$$I_{yy} = \frac{w}{6}\left(l^3\left(1-\frac{l_{cr}}{l}\right)^3\left(1+3\frac{l_{cr}}{l}\right)+{l_b}^3\right)$$

$$\Rightarrow I_{cyy} = \int (x-x_c)^2 dA = \int x^2 dA - {x_c}^2 A_{ABC} = I_{yy} - {x_c}^2 A_{ABC} \tag{21}$$

To illustrate the stresses at the interface *ABC*, first the stresses for the simple pyramidal geometry as depicted in Fig. 2 will be discussed. In Figs. 5 and 6 the normalized stresses τ_{ABC}/p_{pl} and σ_{ABC}/p_{pl} will be shown as a function of the normalized asperity height $\overline{h}$ by varying the normalized asperity width $\overline{w}$. The stress p_{pl}, which is the normal stress on face *BCD*, will be assumed to be equal to H, which is the hardness of the plastically deforming material. According to Tabor, the relation between hardness and yield strength is given by $H \approx 2.8\sigma_y$. As mentioned above, the normal pressure ppl equals to H in the analysis. According the Tresca criterion a material fails as the shear stress exceeds a value equal to $0.5\sigma_y$. So, it follows that the shear stress acting on the ploughing faces has a maximum value according to the situation where the shear stress equals the shear strength of the bulk material

$$\tau_{pl\_max} \approx 0.18 p_{pl} \tag{22}$$

From this analysis it follows that μ has a maximum value of 0.18. The maximum value of μ will only occur in the case of a very good adhesion of the plastic material to the asperity.

The stress component τ_{ABC} is given by Eq. (14) and shown in Fig. 5. From Fig. 5 it becomes clear that τ_{ABC} is strongly related to $\overline{h}$. The influence of $\overline{w}$ is limited. Although the values of $\overline{h}$ and $\overline{w}$ contribute in the same amount to the plastic forces, a higher value of $\overline{w}$ results in a larger area $\overline{A}_{ABC}$ over which the plastic forces can be distributed. So speaking in terms of stresses, the increasing amount of plastic forces due to the increase of $\overline{w}$ is almost

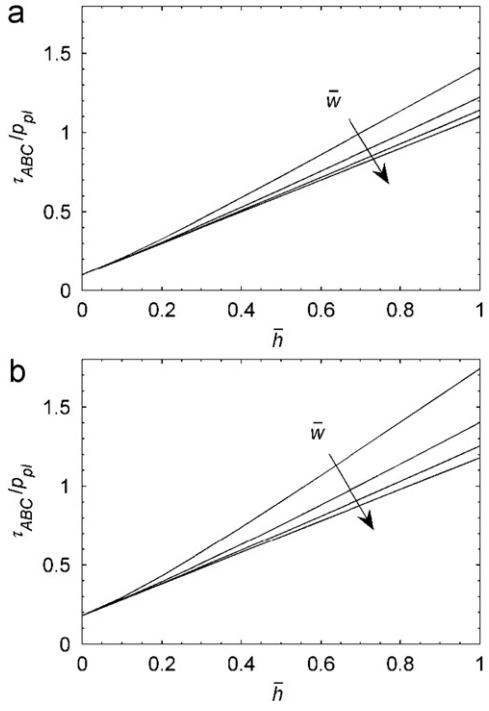

Fig. 5. Mean shear stress over plastic pressure as a function of normalized asperity height on face *ABC* for $\overline{w}=0.25$, 0.5, 1 and lim $\overline{w}\to\infty$ for two different plastic shear strengths: $\mu=0.1$ (a) and $\mu=0.18$ (b). The arrows give the order of the graphs for increasing $\overline{w}$.

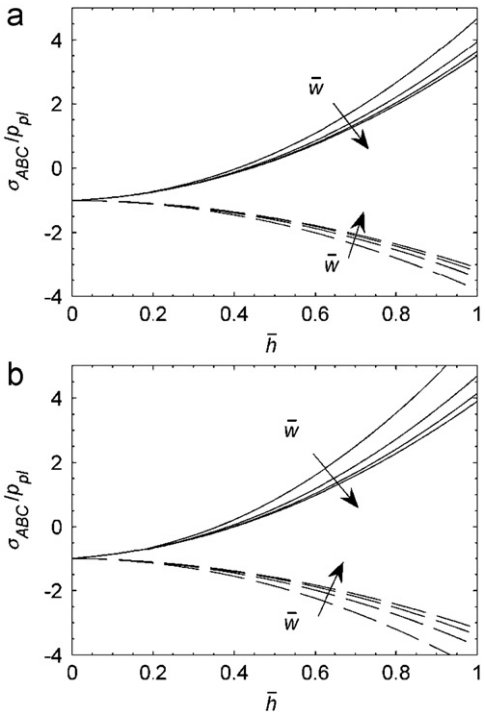

Fig. 6. Normal stress over plastic pressure as a function of normalized asperity height on face *ABC* at $\overline{x}=0$ (dashed lines) and $\overline{x}=1$ (solid lines) for $\overline{w}=0.25$, 0.5, 1 and lim $\overline{w}\to\infty$ for two different plastic shear strengths: $\mu=0.1$ (a) and $\mu=0.18$ (b). The arrows give the order of the graphs for increasing $\overline{w}$.

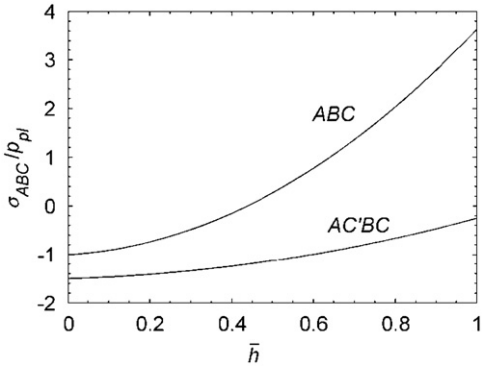

Fig. 7. Normal stress over plastic pressure as a function of normalized asperity height on faces *ABC* and *AC'BC*. The conditions are: $\overline{x}=1$ for $\overline{w}=1$ and $\mu=0.1$.

cancelled out by the larger bearing area of *ABC*. The effect of μ is of importance for values of $\overline{h} \ll 1$. If $\overline{h}=0$ only adhesive forces act on the asperity, so $\tau / p_{pl}=\mu$ for $\overline{h}=0$. For higher values of, $\overline{h}$ the effect of the frontal area, and so the ploughing effect, dominates the plastic forces.

The stress component σ_{ABC} is given by Eq. (15) and shown in Fig. 6. Eq. (15) is a linear function of the $\overline{x}$-coordinate, so the extremes of σ_{ABC} can be found on the extreme $\overline{x}$-coordinates $\overline{x}=0$ and $\overline{x}=1$. For a number of situations, graphs of σ_{ABC} are given for these points in Fig. 6. For $\overline{h} \ll 1$, from $\overline{x}=0$ to $\overline{x}=1$ σ_{ABC} is about equal to the contact pressure. For larger values of $\overline{h}$, the effect of the bending moment with respect to $\overline{x}=\overline{x}_c$ becomes more and more dominant. In Fig. 6, this effect follows from the lines of $\overline{x}=0$ and $\overline{x}=1$ that diverge for increasing $\overline{h}$.

The results for the asperity with the extended base, as depicted in Fig. 3 is shown in Fig. 7. From the graphs it becomes clear that the ratio σ_{ABC}/p_{pl} gets a value in the order of -1 for a wide range of $\overline{h}$. That means that at values of $\overline{h}$ of about 1, using *AC'BC* as the

base of the asperity, the stresses are much lower than in the case that *ABC* is used as base. But for values of $\overline{h}$, let say $\overline{h}<0.2$, *ABC* will give better results than *AC'BC* as the asperity base. The reason is that in the case of small values of $\overline{h}$ the stress state should be close to the contact stress, so σ_{ABC}/p_{pl} should be close to -1. Using *AC'BC* results in a higher compressive stress, namely $\sigma_{ABC}/p_{pl}\approx -1.5$ for $\overline{h}\ll 1$. This stress is the result of the lever effect of the extended rigid asperity. This lever effect is not realistic in the case of low values of $\overline{h}$. A low value of $\overline{h}$ gives not enough stiffness to justify the assumption of a rigid asperity. From Fig. 7 it can be concluded that the part of the base that carries the load is influencing the stresses significantly.

So far, the size of the extended base is unknown. Therefore, FEM calculations will be performed in order to estimate the load carrying area. The asperity is build from elastic tetrahedral elements and calculations are performed for both a rigid and an elastic support of the asperity. The faces *BDC* and *ACD* are loaded with a unit normal pressure that represents the plastic normal load. The plastic shear stress gets the value μ. This way of loading corresponds to normalizing the plastic stresses by p_{pl}. Calculations are performed for different values of $\overline{w}$ and $\overline{h}$ and in Fig. 8 the normalized shear stress at face *ABC* is depicted.

From Fig. 8. it follows that the area that actually carries the load is a function of $\overline{h}$. The stresses in the figure given for the three asperities with the same height ($\overline{h}=0.2$) distribute the load in almost the same manner over the face *AC'BC*. The lower asperity ($\overline{h}=0.1$) has a lower shear stress on this face and less distributed in backwards direction. From these calculation it is concluded that the area on the *xy*-plane that carries (mainly) the load is the quadrilateral *AEBC*, see Fig. 3. Vertex *E* has coordinates $(-l_b, 0, 0)$. The value of l_b as a function of h can be approximated by $l_b=ch$, where c is a constant that has a value of about 2. The stress level is low beyond $\overline{x}<c\overline{h}$ and the shear stress τ_{ABC} is approximated well by Eq. (14) as is shown by the dashed lines in Fig. 8. The value of c has been obtained from FEM simulations for $\overline{h}<0.3$ which is a reasonably high value for the height of the asperity. The value of l_b has the geometrical restriction that *E* remains within the base *AC'BC*. For approximating the internal stresses in the asperity, the focus is fully on the pyramid *AEBCD*. The role of *AC'BED* is negligible.

2.3. Modelling asperity failure

To define a fail criterion relations like Von Mises or Tresca could be used. These relations need the complete stress state. However, here a simplified approach is taken. The stress components σ_{zz} and τ_{xz} are relatively easy to obtain as mentioned above. According the FEM analyses the values of σ_{xx} and σ_{yy} are about a half of the value of σ_{zz}. Shear stress τ_{xy} has a relative small value, about a tenth of τ_{xz}, while τ_{yz} has values in the order of τ_{xz} [6]. Both, τ_{xy} and τ_{yz} are zero on the *xz*-plane due to symmetry. Though, four of the six components are only described qualitatively, a stress criterion can still be given. If a plastic failure is assumed, plastic deformation can be described using the relation of Prandl-Reuss [20] which is valid for the situation that the Von Mises stress exceeds σ_y. In index notation, this relation is given as

$$d\varepsilon_{ij}=\frac{1}{E}\left[(1+\nu)d\sigma_{ij}-\nu\delta_{ij}d\sigma_{kk}\right]+(\sigma_{ij}-1/3\sigma_{kk}\delta_{ij})\,d\lambda \tag{23}$$

In Eq. (23), the deviation of strain is given as a function of the deviation of stresses (elastic effect) and the stresses itself (plastic effect). In this relation E is Young's modulus, ν is Poisson's ratio and δ is the Kronecker delta. The term $d\lambda$ relates the plastic deformation velocity to the stresses and is here only used as a constant without further explanation. According this relation, shear strain with indices ij is only related to other tensor components with indices ij, so independent of tensor components with different indices. That makes the three shear strain equations independent relations. The normal strains are coupled by the effect of the hydrostatic pressure, as given by the terms with δ_{ij}.

To formulate the normal strain relations, the following is assumed:

- The material in the surface is fixed in the x and y directions by its surrounded material. Therefore: $d\varepsilon_{11}=d\varepsilon_{22}=0$. In z-direction the material can be pressed into the contact.
- The load in z-direction is constant: $\sigma_{33}=p_{pl}$. Therefore: $d\sigma_{33}=0$.

(To remain close to the index notation as given in Eq. (23), the indices x, y and z are temporarily replaced by 1, 2 and 3.)

Now, the following set of equations can be derived:

$$\begin{Bmatrix} d\sigma_{11} \\ d\sigma_{22} \end{Bmatrix} = -\frac{Ed\lambda}{3(1-\nu^2)}\begin{bmatrix} 1 & \nu \\ \nu & 1 \end{bmatrix}\left(\begin{bmatrix} 2 & -1 \\ -1 & 2 \end{bmatrix}\begin{Bmatrix} \sigma_{11} \\ \sigma_{22} \end{Bmatrix}+\begin{Bmatrix} p_{pl} \\ p_{pl} \end{Bmatrix}\right) \tag{24}$$

The amplitude of Eq. (24), is not known, because of the unknown $d\lambda$, but still the direction of the deformation can be determined, as is given in the vector plot of Fig. 9. In this figure only the stresses

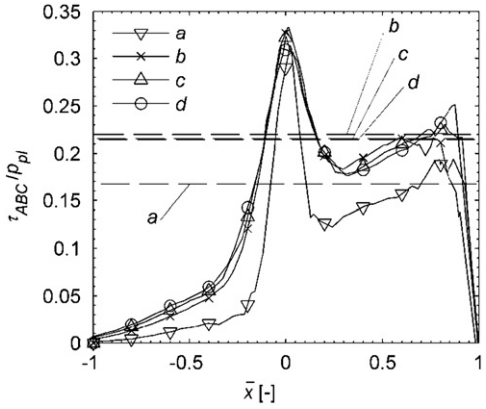

Fig. 8. Shear stress over plastic pressure along the *x*-axis on face *AC'BC*. Comparison of the analytical model (dashed lines) and FEM calculation (lines with markers). The sign of FEM calculations is changed in the plot, in fact, in the plot is given $(-\sigma_{xz}/p_{pl})$. The presented situations that are: $\overline{h}=0.1$, $\overline{w}=1$ (a); $\overline{h}=0.2$, $\overline{w}=0.5$ (b); $\overline{h}=0.2$, $\overline{w}=1$ (c) and $\overline{h}=0.2$, $\overline{w}=2$ (b).

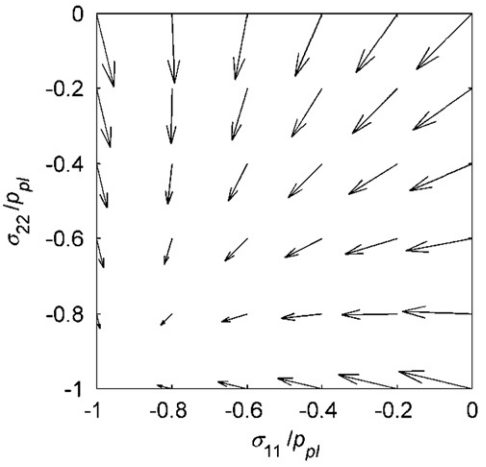

Fig. 9. Vector plot of the stress deviation as a function of the stresses in x and y directions in the case of plastic deformation in the contact zone of an asperity.

are given that are in the range $-1<\sigma/p_{pl}<0$, because the stresses are, according the FEM calculations, in this range before plastic deformation. According to Fig. 9, the deformation is directed to a pure hydrostatic pressure situation. The strain before the hydrostatic pressure situation is reached is very small. In the case of the hydrostatic pressure only, the stresses are fully elastic. Contact pressures are in the order of 1 GPa (a typical hardness value), E is in the order of 200 GPa, so the hydrostatic situation is already reached after a deformation in the order of one per cent.

The next step is the effect of the shear strain components. According to Eq. (23), a strain component ε_{ij}, with $i\neq j$, is only a function of the stress components σ_{ij} and $d\sigma_{ij}$ and is not coupled to stresses with other indices. So, the equations for the shear strain components form a set of uncoupled equations and the effect of every separate shear stress component can be discussed on its own, as will be done below.

- The deformation due to σ_{12} is relatively small, because its value is much smaller as the other components, so its relevance is limited.
- The deformation due to σ_{13} is of importance, because its value is not small related to the other stresses and there is no stabilization after plastic deformation, because shearing in backwards direction of the asperity does not give a fundamental change in the load situation.
- In case of σ_{23} the stress is negative for positive y-coordinates and positive for negative y-coordinates. That means that the material is compressed, so this stress causes a stabilizing action.

From the analysis as described above it follows that most stress components generate a plastic deformation into the direction of a more stable situation. This stabilization is already realized after small deformations. This statement does not hold for σ_{13}. Therefore, this stress will used as the failure criterion for an asperity or a lump on an asperity. The stress field at failure is in fact similar to the stress field at the shakedown limit when analysing shakedown problems, see [21]. Also in such cases this shear stress will be limiting because other stresses can be reduced by residual stresses. So, when according to σ_{13} the asperity deforms plastically, it is stated that it fails. This stress will be calculated using Eq. (14).

3. Modelling shearing of the lump

In the previous section it is concluded that Eq. (14) is a good estimator for asperity failure. Therefore, it will be used as a fail criterion in the analysis. The implementation of this criterion will be discussed in this section.

In the following, the general case for a pyramidal asperity including an extended base and a crack close to point C will be studied. This means that:

$$\overline{A}_{ABC}=(1+c\overline{h}-\overline{l}_{cr}{}^2)\overline{w} \tag{25}$$

Using Eq. (25) in Eq. (14), the following inequality can be constructed:

$$T\geq\frac{1}{1+c\overline{h}-\overline{l}_{cr}{}^2}\left(\overline{h}+\mu\sqrt{1+(\overline{h}/\overline{w})^2}\right) \tag{26}$$

In this equation, μ is defined as the dimensionless shear strength of the ploughing face of the asperity and T is the dimensionless shear strength of the asperity itself. In both cases these shear strengths have been normalized with the normal pressure p_{pl}, so

$$\mu=\frac{\tau_{int}}{p_{pl}} \tag{27}$$

$$T=\frac{\tau_{asperity}}{p_{pl}} \tag{28}$$

The structure of inequality (26) is derived from the plastic force divided by a bearing area. Rewriting this inequality to a form that gives a more direct insight in the dependency of $\overline{h}$ results in

$$(1-\overline{l}_{cr}{}^2)T+(cT-1)\overline{h}\geq\mu\sqrt{1+(\overline{h}/\overline{w})^2} \tag{29}$$

The formulation of inequality (27) gives at the left hand side the force that can be carried at the adapted area of $\overline{A}_{ABC}$ minus the force due to the plastic normal pressure. At the right hand side remains the force due to the plastic shear stress at the interface between the tip and plastic deforming material. This reformulation gives a linear function of $\overline{h}$ crossing a square root function of $\overline{h}$ and shows better the effect of c, $\overline{l}_{cr}$ and μ. Treating Eq. (29) as an equality, it can have at most two solutions, called here as $\overline{h}_{min}$ and $\overline{h}_{max}$

$$\overline{h}_{min}=\frac{T(1-cT)(1-\overline{l}_{cr}{}^2)+\mu\sqrt{T^2(1-\overline{l}_{cr}{}^2)^2/\overline{w}^2+(1-cT)^2-\mu^2/\overline{w}^2}}{(1-cT)^2-\mu^2/\overline{w}^2} \tag{30}$$

$$\overline{h}_{max}=\frac{T(1-cT)(1-\overline{l}_{cr}{}^2)-\mu\sqrt{T^2(1-\overline{l}_{cr}{}^2)^2/\overline{w}^2+(1-cT)^2-\mu^2/\overline{w}^2}}{(1-cT)^2-\mu^2/\overline{w}^2} \tag{31}$$

The limit situation for $|1-cT|=\mu/\overline{w}$ reads

$$\overline{h}_{max}=\frac{\overline{w}}{2}\left|\frac{(1-\overline{l}_{cr}{}^2)T}{\mu}-\frac{\mu}{(1-\overline{l}_{cr}{}^2)T}\right| \tag{32}$$

The possible solutions of inequality (29) for several cases are given in Tables 1 and 2.

For the situation that $\overline{l}_b=c\overline{h}$ exceeds the value of 1, Eq. (25) is not valid anymore, because $\overline{A}_{ABC}$is limited by the area of $AC'BC$. This results in a limitation of $\overline{h}$ to

$$\overline{h}\leq\frac{T(2-\overline{l}_{cr}{}^2)-\mu\sqrt{T^2(2-\overline{l}_{cr}{}^2)^2/\overline{w}^2+1-\mu^2/\overline{w}^2}}{1-\mu^2/\overline{w}^2} \tag{33}$$

Table 1
Solutions of inequality (27) for different situations.

	$cT<1$	$cT=1$	$cT>1$
$\mu=0$	$\overline{h}\leq\overline{h}_{max}$	No maximum of $\overline{h}$	No maximum of $\overline{h}$
$\mu<(1-\overline{l}_{cr}{}^2)T$	$\overline{h}\leq\overline{h}_{max}$	$\overline{h}\leq\overline{h}_{max}$	See Table 2
$\mu\geq(1-\overline{l}_{cr}{}^2)T$	$\overline{h}=0$	$\overline{h}=0$	See Table 2

Table 2
Solutions of inequality (27), detail of Table 1 for $cT>1$ and $\mu>0$.

	$\mu<(1-\overline{l}_{cr}{}^2)T$	$\mu\geq(1-\overline{l}_{cr}{}^2)T$
$\mu/\overline{w}\leq cT-1$	No maximum of $\overline{h}$	$\overline{h}\geq\overline{h}_{min}$
$(cT-1)^2<(\mu^2/\overline{w}^2)\leq(cT-1)^2+((1-\overline{l}_{cr}{}^2)^2T^2/\overline{w}^2)$	$\overline{h}\leq\overline{h}_{max}$	$\overline{h}_{min}\leq\overline{h}\leq\overline{h}_{max}$
$(\mu^2/\overline{w}^2)>(cT-1)^2+((1-\overline{l}_{cr}{}^2)^2T^2/\overline{w}^2)$	$\overline{h}\leq\overline{h}_{max}$	$\overline{h}=0$

As long as the inequalities (29) and (33) are met, the asperity will resist the plastic forces, otherwise it fails. This gives a criterion of the maximum possible value of $\overline{h}$ for the pyramidal asperity.

4. Results

In Figs. 10 and 11 a number of results are shown. The dotted lines in the figures show the transitions between different wear regimes as described, for reference, in the wear mode diagram of Hokkirigawa and Kato [5], also shown in Fig. 1, but now presented in terms of μ and $\overline{h}_{max}$ instead of the original variables θ and f_{HK} using the relations $\mu=0.18\,f_{HK}$ and $\overline{h}=\tan\theta$. From Figs. 10 and 11 the effect of the T and m on the maximum height $\overline{h}_{max}$ is shown. The effect of μ becomes clear in all graphs. An increasing value of μ results in an increasing force on the tip, so the maximum height of the asperity at which no failure occurs, reduces.

Parameter T which is the shear strength of the asperity over the hardness of the soft counter surface, is another quantity that has a strong effect on the maximum tip height. From Table 1 it follows that for the case that the tip material has the same strength as the plastic material through which it ploughs, so $T=0.18$, the asperity will shear immediately if $\mu>0.18$, so $\overline{h}_{max}=0$. This is an obvious result, since this case corresponds to a ploughing asperity with a shear strength of the tip that is equal to the shear strength of the soft counter surface loaded by a shear stress at the ploughing faces equal to the shear strength of the soft counter surface. So in fact, this case is the case of internal shear in the bulk, see also Eq. (22). Further, if μ is decreased, e.g. by boundary layers, this has a strong effect on the maximum height at which the asperity is still stable.

In case that $cT\geq 1$ and $\mu=0$, $\overline{h}$ has no maximum, according to Table 1. However, if inequality of Eq. (33) is taken into account, $\overline{h}$ has always a maximum. The effect of inequality according to Eq. (33) is visible in Figs. 10 and 11 as the difference in the dashed and solids graphs. From the graphs in Fig. 10a the significant effect of T becomes clear, but the effect is weakened by inequality of Eq. (33). Below $T=0.2$ the cutting and wedging regimes will, for the assumed values, not be entered because the asperity will shear.

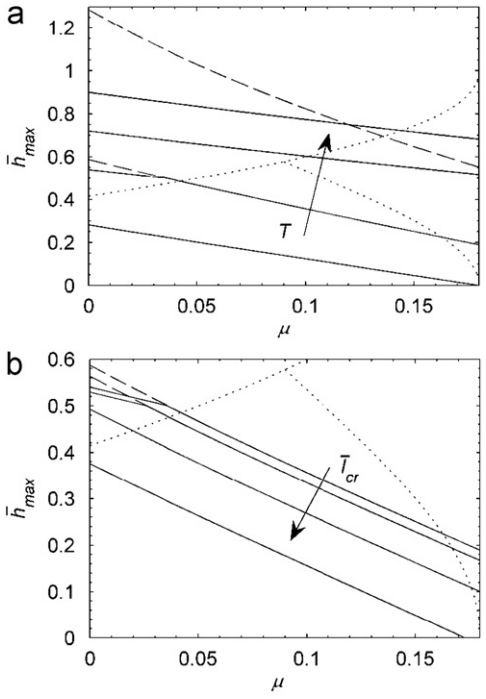

Fig. 10. Maximum possible values of $\overline{h}$ as a function of the plastic coefficient of friction for different properties of the asperity. The default values are $T=0.27$, $\overline{l}_{cr}=0$, $c=2$ and $\overline{w}=1$. The varied variables increase in the direction of the arrows. The dashed lines show the graphs in the case that the constraint of inequality (31) was not used. The variations are: (a) $T=0.18$, 0.27, 0.36 and 0.45. The 'free' dashed line belongs to $T=0.36$ and the dashed line of $T=0.45$ is omitted, because it lies far above the other graphs. (b) Results for $\overline{l}_{cr}=0$, 0.2, 0.4 and 0.6.

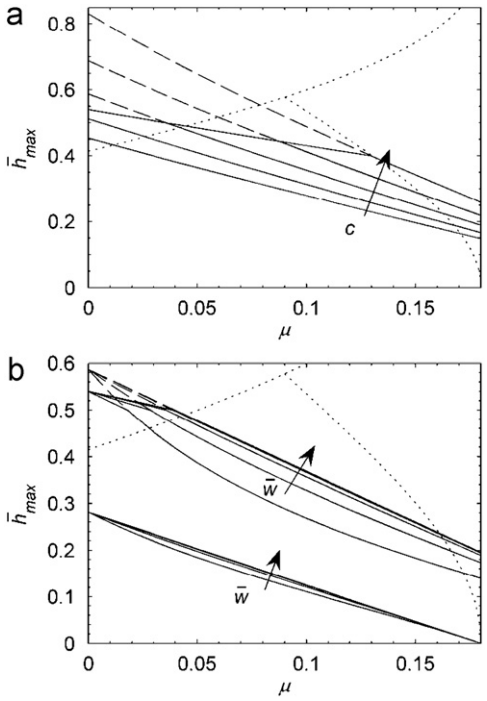

Fig. 11. Maximum possible values of $\overline{h}$ as a function of the plastic coefficient of friction for different properties of the asperity. The default values are $T=0.27$, $\overline{l}_{cr}=0$, $c=2$ and $\overline{w}=1$. The varied variables increase in the direction of the arrows. The dashed lines show the graphs in the case that the constraint of inequality (31) was not used. The variations are: (a) $c=1.5$, 1.75, 2, 2.25 and 2.5. (b) $\overline{w}=0.25$, 0.5, 1, 2 and 4.

The effect of the crack size is shown in Fig. 10b. For the given situation, An increasing crack length $\overline{l}_{cr}$ reduces the maximum value of $\overline{h}$. An almost linear relation exists between the crack area size and the maximum tip height.

In Fig. 11a the effect of the factor c, describing the extend of load carrying area, is presented. In fact this factor is a constant that is determined by FEM-calculations as discussed above. The figure shows the sensitivity of this estimation. As long as inequality (31) has no effect, the factor c has a clear effect. In the case that inequality (31) restricts $\overline{h}$, c has a minor effect.

The width $\overline{w}$ of the asperity has a weak effect on the maximum value of $\overline{h}$. In Fig. 11b a large range of $\overline{w}$ is presented. Only for small values of $\overline{w}$, so, $\overline{w}<1$, the effect of $\overline{w}$ is clearly visible. In inequality (27) $\overline{w}$ is incorporated in the term $\overline{h}/\overline{w}$. The effect of this term is shown in Fig. 11b by the sets of graphs for different values of T. A higher value of T result in a higher value of $\overline{h}$ and so in a stronger effect of $\overline{w}$. For even higher values of T as presented in Fig. 11b, the effect of $\overline{w}$ would be stronger according to inequality (27), but is mostly restricted by the constraint of inequality (31). This means that the width of the ploughing pyramid will not affect it sensitivity for yielding strongly. From the graphs and the analysis it can be concluded that μ and T are the most important variables for using the model.

In Fig. 12, results are presented that are comparable with Figs. 10 and 11. Two values of μ have been chosen, respectively 0,05 and 0.18 where 0.05 would correspond to a well lubricated contact and 0.18 to an unlubricated contact. The choice of the

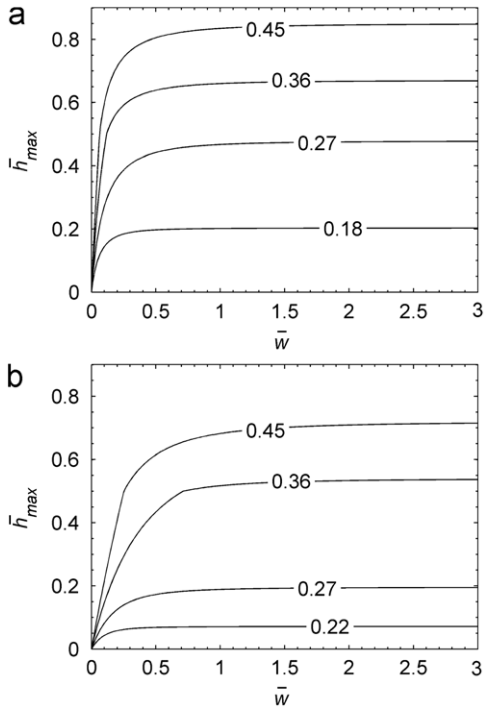

Fig. 12. Maximum possible values of $\bar{h}$ as a function of $\bar{w}$ for different values of T (given by the values on the graphs) and $\bar{l}_{cr}=0$ and $c=2$ for: (a) $\mu=0.05$ and (b) $\mu=0.18$.

axes is such that they are comparable with the presentation of experimental results in [22]. An individual graph can be interpreted as representing a tribological contact, so a given hardness difference between the contacting bodies as represented by T and a given value of μ. The graph gives the maximum value of $\bar{h}$ for all asperities, each with each their own value of $\bar{w}$. From this figure, again, it follows that the maximum value of $\bar{h}$ of an asperity is strongly related to T. It can be seen that at lower values of T, the height is also dependent on μ. For $\bar{w}<0.5$, $\bar{w}$ has a strong influence on the maximum value of $\bar{h}$. For higher values of T, the effect of $\bar{w}$ is negligible.

5. Discussion

Based on the results describe above, some consequences can be discussed in the context of adhesive and abrasive wear processes. According to [23] material transfer from the sheet to the tool in a deep drawing process occurs in the wedge regime. Combining the results of the maximum $\bar{h}$ of lumps on the tool surface and the wear mode diagram, some things can observed. For entering the wedge formation regime, μ should be higher than 0.09, which corresponds to $f_{HK}>0.5$. From Fig. 10a it follows that $\bar{h}$ cannot exceed 1 due to lump growth in the wedge formation regime. For values of μ a bit higher than 0.09, lump growth takes place in a very narrow band of $\bar{h}$-values. For values of μ of about 0.18, lump growth can occur in a large range of $\bar{h}$ and for $\mu=0.18$ for $\bar{h}<1$ (so, practically for every asperity) lump growth will occur. So, a higher value of μ gives more risk of galling as does a higher roughness of the tool, which corresponds to a higher value of $\bar{h}$. Further, lumps will harden on the tool surface due to excessive plastic deformation. If the resulting hardness of the lump is much higher than the original hardness of the counter surface, high lumps can develop because of high values of T. So higher lumps are expected for materials which are more able to work harden. Further, in the case of plastic (tensile) bulk deformation of the sheet in a deep drawing process, the effective hardness of the sheet (so the soft counter surface) decreases, see e.g. [24]. So, in areas of e.g. a deep drawing process where the in-plane strains are high, the value of T will increase, lumps can increase more in height, and a potentially higher damage to the sheet may occur. These effects are in agreement with industrial experience, see. e.g. [25].

In the case of abrasion processes, a rule of thumb is that above 20% hardness difference between the surfaces abrasive action occurs. A hardness difference of 20% between the ploughing asperity and the soft counter surface results in a $T\sim0.22$. From Fig. 10a it follows that for a certain value of μ say 0.05, the maximum value of $\bar{h}$ is around 0.2. So, according to the model, any asperity with an attack angle larger than about 12° will shear. This critical angle is almost independent of the width of the ploughing asperities, as can be seen in Fig. 11b. It can be seen that this model is in agreement with the rule of thumb at only at sufficient hardness difference around 20% between contacting surfaces abrasion occurs, meaning that the abrasive itself is mechanically stable and will not fail. The 20% is a rule of thumb, so it should not be strongly dependent on the geometry of the ploughing asperities. This is in agreement with the model where, given a certain attack angle, the width of the asperity is also not at large influence.

6. Conclusions

A model has been developed describing plastic failure of ploughing asperities with a four sided base. Simple criteria have been derived which describe limits to the geometry of ploughing the asperities. Above these limits, failure of the asperity by the ploughing forces will occur. In the analysis, it has been shown that shear of ploughing asperities will be predominantly determined by the lateral shear stress in the asperity only.

For failure, in particular the shear strength of the asperity as related to the hardness of the soft surface, has a high influence. Also, the coefficient of friction, so the shear strength at the ploughing face as related to the hardness of the soft surface, has an important influence. Contrary to this, the width of the asperity has a minor influence on failure of the asperity. The developed criteria can be used to determine stable lump shapes which are building up on surfaces due to material transfer in adhesive wear situations. Further, the results can be used to analyse asperity failure in two body abrasive wear processes.

Acknowledgements

This research was carried out under the project number MC1.03160 in the framework of the Research Program of the Materials innovation institute (M2i) (www.m2i.nl), which is greatly appreciated.

Appendix A

Here, expressions for σ_{ABC} and τ_{ABC} will be derived for the geometry shown in Fig. 2. The equation of equilibrium in the x-direction results in the following equation:

$$\sum F_x = 0 \Rightarrow -\int p_{pl}\vec{n}\cdot\vec{x}\,dA+\int \tau_{pl}\vec{t}\cdot\vec{x}\,dA+\int \tau_{ABC}\,dA=0$$

$$\Leftrightarrow -p_{pl}wh-\tau_{pl}l\sqrt{w^2+h^2}+\tau_{ABC}A_{ABC}=0 \quad (A.1)$$

From these equations follows the value of τ_{ABC}

$$\tau_{ABC}=\frac{1}{A_{ABC}}(p_{pl}wh+\tau_{pl}l\sqrt{w^2+h^2})=\frac{p_{pl}}{A_{ABC}}(wh+\mu l\sqrt{w^2+h^2}) \quad (A.2)$$

Equilibrium in the z-direction results in

$$\begin{aligned}\sum F_z=0 \Rightarrow & -\int p_{pl}\vec{n}\cdot\vec{z}\ dA+\int \tau_{pl}\vec{t}\cdot\vec{z}\ dA\\ & +\int \sigma_{ABC}(x)\vec{n}\cdot\vec{z}\ dA=0\\ \Leftrightarrow & -p_{pl}wl+\tau_{pl}\frac{w^2h}{\sqrt{w^2+h^2}}+C\delta_cA_{ABC}=0\end{aligned} \quad (A.3)$$

Here, the symbol δ_c represents the value of the virtual displacement δ at location $x=x_c$, where x_c is the x-coordinate of the centroid of face ABC. From equilibrium in the z-direction σ_{ABC} cannot be determined over the whole face ABC, but using Eq. (10) it can be derived that δ_c is proportional to the mean value of σ_{ABC}. This gives the following:

$$\delta_c=\frac{1}{CA_{ABC}}\left(p_{pl}wl-\tau_{pl}\frac{w^2h}{\sqrt{w^2+h^2}}\right)=\frac{p_{pl}}{CA_{ABC}}\left(wl-\mu\frac{w^2h}{\sqrt{w^2+h^2}}\right) \quad (A.4)$$

The equation of moment equilibrium around to the y-axis results in

$$\begin{aligned}M_{yy}=\left(\int \vec{r}\times d\vec{F}\right)\cdot\vec{y}=\int z\,dF_x-\int x\,dF_z=0\\ \Rightarrow -\int zp_{pl}\vec{n}\cdot\vec{x}\ dA+\int xp_{pl}\vec{n}\cdot\vec{z}\ dA+\int z\tau_{pl}\vec{t}\cdot\vec{x}\ dA\\ -\int x\tau_{pl}\vec{t}\cdot\vec{z}\ dA-\int x\sigma_{ABC}\vec{n}\cdot\vec{z}\ dA=0\\ \Leftrightarrow \tfrac{1}{3}p_{pl}w(l^2-h^2)-\frac{\tau_{pl}l}{3}\left(h\sqrt{w^2+h^2}+\frac{w^2h}{\sqrt{w^2+h^2}}\right)\\ -C(\delta_cx_cA_{ABC}+I_{cyy}\theta)=0\end{aligned} \quad (A.5)$$

In (A.5) $\vec{r}$ and $\vec{F}$ are respectively the location and the force vector. In the last equation I_{cyy} means the area moment of inertia of face ABC with respect to the line $x=x_c$. From vertical and moment equilibrium, so Eqs. (A.4) and (A.5), it follows:

$$\theta=\frac{p_{pl}}{3CI_{cyy}}\left(w(l^2-h^2-3x_cl)+\frac{\mu h}{\sqrt{w^2+h^2}}(3x_cw^2-l(2w^2+h^2))\right) \quad (A.6)$$

The normal stress σ_{ABC} can be found by substituting Eq. (A.4) and (A.6) in Eq. (10). In dimensionless form the final result is obtained

$$\frac{\tau_{ABC}}{p_{pl}}=\frac{1}{\bar{A}_{ABC}}\left(\bar{w}\bar{h}+\mu\sqrt{\bar{w}^2+\bar{h}^2}\right) \quad (A.7)$$

$$\begin{aligned}\frac{\sigma_{ABC}}{p_{pl}}=&-\frac{\bar{w}}{\bar{A}_{ABC}}\left(1-\frac{\mu\bar{w}\bar{h}}{\sqrt{\bar{w}^2+\bar{h}^2}}\right)+\frac{1}{3\bar{I}_{cyy}}\\ &\times\left(\bar{w}(\bar{h}^2-1+3\bar{x}_c)+\frac{\mu\bar{h}(2\bar{w}^2+\bar{h}^2-3\bar{x}_c\bar{w}^2)}{\sqrt{\bar{w}^2+\bar{h}^2}}\right)(\bar{x}-\bar{x}_c)\end{aligned} \quad (A.8)$$

References

[1] M.A. Masen, M.B. de Rooij, D.J. Schipper, Micro-contact based modelling of abrasive wear, Wear 258 (2005) 339–348.
[2] X. Ma, M.B. de Rooij, D.J. Schipper, A load dependent friction model for fully plastic contact conditions, Wear 269 (2010) 790–796.
[3] J.A. Williams, Wear modelling: analytical, computational and mapping: a continuum mechanics approach, Wear 225–229 (1999) 1–17.
[4] J.M. Challen, P.L.B. Oxley, An explanation of the different regimes of friction and wear using asperity deformation models, Wear 53 (1979) 229–243.
[5] K. Hokkirigawa, K. Kato, An experimental and theoretical investigation of ploughing, cutting and wedge formation during abrasive wear, Tribology International 21 (1988) 51–57.
[6] G. van der Linde, Predicting Galling Behaviour in Deep Drawing Processes, Ph.D. Thesis, University of Twente, The Netherlands, 2011.
[7] J.M. Challen, P.L.B. Oxley, E.D. Doyle, The effect of strain hardening on the critical angle for abrasive (chip formation) wear, Wear 88 (1983) 1–12.
[8] T. Abildgaard, Prediction of the force components acting on a ploughing cone by means of three-dimensional upper bound theory, Advanced Technology of Plasticity 1 (1984) 121–126.
[9] M. DeVathire, F. Delamare, E. Felder, An upper bound model of ploughing by a pyramidal indenter, Wear 66 (1981) 51–64.
[10] A. Azarkhin, M.L. Devenpeck, Enhanced model of a plowing asperity, Wear 206 (1997) 147–155.
[11] A.A. Torrance, The influence of surface deformation on mechanical wear, Wear 200 (1996) 45–54.
[12] L. Zhang, H. Tanaka, Towards a deeper understanding of wear and friction on the atomic scale—a molecular dynamics analysis, Wear 211 (1997) 44–53.
[13] J.B. Adams, L.G. Hector Jr., D.J. Siegel, H. Yu, J. Zhong, Adhesion, lubrication and wear on the atomic scale, Surface and Interface Analysis 31 (2001) 619–626.
[14] J. Zhong, J.B. Adams, L.G. Hector, Molecular dynamics simulations of asperity shear in aluminum, Journal of Applied Physics 94 (2003) 4306–4314.
[15] V.L. Popov, S.G. Psakhie, Numerical simulation methods in tribology, Tribology International 40 (2007) 916–923.
[16] K.L. Johnson, The correlation of indentation experiments, Journal of the Mechanics and Physics of Solids 18 (1970) 11–126.
[17] K.L. Johnson, Contact mechanics and the wear of materials, Wear 190 (1995) 162–170.
[18] T. Kayaba, K. Hokkirigawa, K. Kato, Experimental analysis of the yield criterion for a hard asperity sliding over a soft surface, Wear 96 (1984) 255–265.
[19] T. Kayaba, K. Hokkirigawa, K. Kato, Theoretical analysis of the yield criterion for a hard asperity sliding over a soft surface, Wear 87 (1983) 151–161.
[20] J. Chakrabarty, Theory of Plasticity, third ed., Elsevier, Amsterdam, 2006.
[21] A. Kapoor, K.L. Johnson, Effect of changes in contact geometry on shakedown of surfaces in rolling/sliding contact, International Journal of Mechanical Sciences 34 (1992) 223–239.
[22] K. Kato, K. Hokkirigawa, T. Kayaba, Y. Endo, Three dimensional shape effect on abrasive wear, Journal of Tribology 108 (1986) 346–351.
[23] M.B. de Rooij, D.J. Schipper, Analysis of material transfer from a soft workpiece to a hard tool—part I—lump growth model, Journal of Tribology 123 (2001) 469–473.
[24] W.R.D. Wilson, S. Sheu, Real area of contact and boundary friction in metal forming, International Journal of Mechanical Sciences 30 (1988) 475–489.
[25] E. Schedin, B. Lethinen, Galling mechanisms in lubricated systems: a study of sheet metal forming, Wear 170 (1993) 119–130.